



**HAL**  
open science

## **A new method of reconstructing the P-T conditions of fluid circulation in an accretionary prism (Shimanto, Japan) from microthermometry of methane-bearing aqueous inclusions**

Hugues Raimbourg, Régis Thiery, Maxime Vacelet, Claire Ramboz, Nicolas Cluzel, Emmanuel Le Trong, Asuka Yamaguchi, Gaku Kimura

### ► To cite this version:

Hugues Raimbourg, Régis Thiery, Maxime Vacelet, Claire Ramboz, Nicolas Cluzel, et al.. A new method of reconstructing the P-T conditions of fluid circulation in an accretionary prism (Shimanto, Japan) from microthermometry of methane-bearing aqueous inclusions. *Geochimica et Cosmochimica Acta*, 2014, 125, pp.96-109. 10.1016/j.gca.2013.09.025 . insu-00873933

**HAL Id: insu-00873933**

**<https://insu.hal.science/insu-00873933>**

Submitted on 19 Nov 2013

**HAL** is a multi-disciplinary open access archive for the deposit and dissemination of scientific research documents, whether they are published or not. The documents may come from teaching and research institutions in France or abroad, or from public or private research centers.

L'archive ouverte pluridisciplinaire **HAL**, est destinée au dépôt et à la diffusion de documents scientifiques de niveau recherche, publiés ou non, émanant des établissements d'enseignement et de recherche français ou étrangers, des laboratoires publics ou privés.

# A new method of reconstructing the $P$ - $T$ conditions of fluid circulation in an accretionary prism (Shimanto, Japan) from microthermometry of methane-bearing aqueous inclusions

Hugues Raimbourg<sup>a,b,\*</sup>, Régis Thiéry<sup>c</sup>, Maxime Vacelet<sup>d</sup>, Claire Ramboz<sup>a</sup>, Nicolas Cluzel<sup>c</sup>, Emmanuel Le Trong<sup>a</sup>, Asuka Yamaguchi<sup>e</sup>, Gaku Kimura<sup>e</sup>

<sup>a</sup>*Univ. d'Orléans, ISTO, UMR 7327, 45071, Orléans, France ; CNRS, ISTO, UMR 7327, 45071 Orléans, France ; BRGM, ISTO, UMR 7327, BP 36009, 45060 Orléans, France*

<sup>b</sup>*IFREE, Japan Agency for Marine-Earth Science and Technology, 2-15 Natsushima-cho, Yokosuka, Kanagawa 237-0061, Japan*

<sup>c</sup>*LMV, Laboratoire Magmas et Volcans, UMR 6524, CNRS/Clermont Université, Clermont-Ferrand, France*

<sup>d</sup>*MINES-Paristech, Centre de Géosciences, 35, rue Saint-Honoré, 77305 Fontainebleau Cedex, France*

<sup>e</sup>*Department of Earth and Planetary Science, The University of Tokyo, 7-3-1 Hongo, Bunkyo-ku, Tokyo 113-0033, Japan*

---

## Abstract

In paleo-accretionary prisms and the shallow metamorphic domains of orogens, circulating fluids trapped in inclusions are commonly composed of a mixture of salt water and methane, producing two types of fluid inclusions: methane-bearing aqueous and methane-rich gaseous fluid inclusions. In such geological settings, where multiple stages of deformation, veining and fluid influx are prevalent, textural relationships between aqueous and gaseous inclusions are often ambiguous, preventing the microthermometric

---

\*Corresponding author

*Email addresses:* [hugues.raimbourg@univ-orleans.fr](mailto:hugues.raimbourg@univ-orleans.fr) (Hugues Raimbourg),  
[r.thiery@opgc.univ-bpclermont.fr](mailto:r.thiery@opgc.univ-bpclermont.fr) (Régis Thiéry)

determination of fluid trapping pressure and temperature conditions.

To assess the  $P$ - $T$  conditions of deep circulating fluids from the Hyuga unit of the Shimanto paleo-accretionary prism on Kyushu, Japan, we have developed a new computational code, applicable to the  $\text{H}_2\text{O}$ - $\text{CH}_4$ - $\text{NaCl}$  system, which allows the characterization of  $\text{CH}_4$ -bearing aqueous inclusions using only the temperatures of their phase transitions estimated by microthermometry:  $T_{mi}$ , the melting temperature of ice;  $T_{\text{hyd}}$ , the melting temperature of gas hydrate and  $T_{h,\text{aq}}$ , homogenization temperature. This thermodynamic modeling calculates the bulk density and composition of aqueous inclusions, as well as their  $P$ - $T$  isochoric paths in a  $P$ - $T$  diagram with an estimated precision of approximately 10 %.

We use this computational tool to reconstruct the entrapment  $P$ - $T$  conditions of aqueous inclusions in the Hyuga unit, and we show that these aqueous inclusions cannot be cogenetic with methane gaseous inclusions present in the same rocks. As a result, we propose that pulses of a high-pressure, methane-rich fluid transiently percolated through a rock wetted by a lower-pressure aqueous fluid. By coupling microthermometric results with petrological data, we infer that the exhumation of the Hyuga unit from the peak metamorphic conditions was nearly isothermal and ended up under a very hot geothermal gradient.

In subduction or collision zones, modeling aqueous fluid inclusions in the ternary  $\text{H}_2\text{O}$ - $\text{CH}_4$ - $\text{NaCl}$  system and not simply in the binary  $\text{H}_2\text{O}$ - $\text{NaCl}$  is necessary, as the addition of even a small amount of methane to the water raises significantly the isochores to higher pressures. Our new code provides therefore the possibility to estimate precisely the pressure conditions of fluids

circulating at depth.

*Keywords:* fluid inclusions, microthermometry, Raman spectroscopy, gas hydrates, H<sub>2</sub>O-CH<sub>4</sub>-NaCl

---

## 1 **1. Introduction**

2 Using observation of thousands of fluid inclusions in quartz veins from the  
3 Central Alps, Mullis (1979) and Mullis et al. (1994) recognized the correspon-  
4 dence of the nature of the fluid with metamorphic grade: Methane-bearing  
5 aqueous fluids are dominant at low metamorphic grade, up to  $\sim 300^\circ$  C. Simi-  
6 larly, water and methane have been identified as the major components of the  
7 fluid in many worldwide paleo-accretionary prisms, including the Shimanto  
8 Belt in Japan (Sakaguchi, 1999a; Lewis et al., 2000; Kondo et al., 2005),  
9 Kodiak Island in Alaska (Vrolijk et al., 1988) and the Franciscan Complex  
10 in California (Dalla Torre et al., 1996; Sadofsky and Bebout, 2004). Fluid  
11 inclusions carry invaluable information regarding pressure ( $P$ ) - temperature  
12 ( $T$ ) conditions of the fluid at the time of trapping and, indirectly, of the host  
13 terrane, in the shallow portion ( $P \sim 0 - 500$  MPa) of subduction and colli-  
14 sion zones where the analysis of complex phase assemblages with the help of  
15 thermodynamic databases and software (e.g. THERMOCALC, (Powell and  
16 Holland, 1988) or TWEEQU (Berman, 1991)) is not possible.

17 To this end, the following procedure (e.g. Alderton and Bevins, 1996),  
18 which is applicable when aqueous inclusions and methane-rich gaseous in-  
19 clusions are simultaneously present, is commonly used (see Table 1 for a list  
20 of symbols): If one assumes that these inclusions were trapped under the  
21 same conditions, then the trapping pressure ( $P_t$ ) and temperature ( $T_t$ ) can

22 be estimated on a  $P$ - $T$  diagram from the intersection of the isochores of  
23 gaseous inclusions with the isotherm  $T = T_{h, \text{aq}}$  of aqueous inclusions (where  
24  $T_{h, \text{aq}}$  is the homogenization temperature of aqueous inclusions). The central  
25 assumption of this method is that the two types of fluid inclusions derive  
26 from the entrapment of the two end-members of an immiscible mixture of a  
27  $\text{CH}_4$  ( $\pm\text{H}_2\text{O}$ ) gas in equilibrium with a dense  $\text{H}_2\text{O}$ - $\text{NaCl}$  ( $\pm\text{CH}_4$ ) solution. In  
28 other words, this method assumes that aqueous and gaseous inclusions are  
29 cogenetic.

30 This assumption is commonly based on the distribution and the geometry  
31 of the inclusions (e.g. primary inclusions of the two kinds trapped in the  
32 same crystal). However, in orogenic settings, where rocks have experienced  
33 multiple stages of deformation and fluid influx, most inclusions are secondary  
34 and textures are often ambiguous.

35 Thus, one must assess if there was a single fluid at depth or if the two  
36 kinds of inclusions correspond to two unrelated fluids, trapped at either the  
37 same or even different  $P$ - $T$  conditions. To this end, an approach alternative  
38 to texture analysis is to determine, from microthermometric measurements,  
39 the possibility for several populations of fluid inclusions to be thermody-  
40 namically in equilibrium (Pichavant et al., 1982; Ramboz et al., 1982). To  
41 prove their cogenetic character, several conditions must be met, including  
42 a similar temperature for total homogenization. This transition is readily  
43 observable in water-rich fluid inclusions by the disappearance of thermally  
44 agitated bubbles of methane. In methane-rich inclusions, the water phase,  
45 occupying a low volume fraction and forming a meniscus on the rim of the  
46 inclusion, is often not visible, hence total homogenization cannot be mea-

47 sured optically. An alternative solution was developed by Mullis (1979), who  
48 showed good agreement between the estimated molar fraction of methane in  
49 water-rich inclusions and the saturation concentration of methane in water for  
50 the  $P$ - $T$  conditions of equilibrium between water-rich and methane-rich fluid  
51 inclusions. This method is nevertheless restricted to exceptionnally large  
52 water-rich fluid inclusions where the density of the bubble of methane can  
53 be estimated with a freezing stage. In general, however, it is often difficult  
54 to check the cogenetic character of methane-rich and water-rich inclusions.

55 The above mentioned difficulties present themselves when working with  
56 aqueous  $\text{H}_2\text{O}$ - $\text{NaCl}$ - $\text{CH}_4$  inclusions in rocks of the Shimanto paleo-accretionary  
57 complex (Japan). In particular, small ( $\sim 5\mu\text{m}$ ), aqueous inclusions are asso-  
58 ciated with some gaseous  $\text{CH}_4$  inclusions, whose cogenetic character cannot  
59 be clearly supported by texture analysis. Unfortunately, such ambiguous  
60 textural relationships are common in orogenic contexts, limiting the scope of  
61 microthermometry in these formations.

62 Regardless, aqueous inclusions exhibit one additional phase transition,  
63 which is the melting of a gas hydrate in the presence of a vapour phase. Its  
64 temperature can be measured by microthermometry, generally between  $0^\circ\text{C}$   
65 and  $15^\circ\text{C}$ , and this data gives us one additional constraint to characterize  
66 aqueous inclusions in terms of bulk content and density. Two models to this  
67 end (Dubessy et al., 1992; Mao et al., 2011) already exist in the literature,  
68 but none can be applied to Shimanto paleo-accretionary complex: Dubessy  
69 et al. (1992) does not take into account  $T_{h,\text{aq}}$ , whereas Mao et al. (2011)  
70 does not take into account the presence of dissolved salts. We have, there-  
71 fore, built a new algorithm allowing the complete characterization of the

72 properties of an aqueous CH<sub>4</sub> and NaCl-bearing aqueous inclusion (i.e. bulk  
73 density, bulk content, isochoric paths) using three measured phase transition  
74 temperatures:  $T_{mi}$ , melting temperature of ice;  $T_{hyd}$ , melting temperature  
75 of gas hydrate and  $T_{h,aq}$ , homogenization temperature. This new model is  
76 described in Section 4 after a discussion of the geological context (Section 2)  
77 and of the microthermometric analysis (Section 3).

78 Section 6 synthesizes the main results, which have been obtained from this  
79 microthermometric work and thermodynamic modeling and shows that the  
80 Hyuga unit has experienced important fluid composition changes in the past  
81 (methane-rich and water-rich fluids in disequilibrium) as well as variations  
82 in thermal regime.

## 83 **2. Geological context**

84 The Hyuga Group is part of the Shimanto Belt on Kyushu, Japan (Fig.  
85 1). This belt is interpreted as a paleo-accretionary complex formed dur-  
86 ing the subduction of the Pacific plate below the Eurasian Plate (Taira  
87 et al., 1988). It is divided by the Nobeoka Tectonic Line (NTL), an out-of-  
88 sequence megathrust, several hundreds of kilometers long, marking a large  
89 stratigraphic and metamorphic gap (Imai et al., 1971; Toriumi and Teruya,  
90 1988).

91 The Hyuga *mélange* is the uppermost unit of the Hyuga Group and consti-  
92 tutes the footwall of the NTL. It was strongly deformed and affected by meta-  
93 morphism, with peak temperature conditions estimated around 250-300°C  
94 on the basis of vitrinite reflectance (Kondo et al., 2005) or illite cristallinity  
95 (Hara and Kimura, 2008; Mukoyoshi et al., 2009). In addition, Mukoyoshi

96 et al. (2009) describe a lateral temperature gradient from the east ( $\sim 250^\circ\text{C}$ )  
97 to the west ( $\sim 280^\circ\text{C}$ ). Furthermore, based on prehnite-pumpellyite meta-  
98 morphic assemblages in greenstones included in the *mélange*, Toriumi and  
99 Teruya (1988) estimated the peak metamorphic conditions as 3-5 kbars and  
100 200-300 $^\circ\text{C}$ .

101 The Hyuga *mélange* has a block-and-matrix structure, where blocks are  
102 made of lenses of sandstone/siltstone or early stage quartz veins and matrix is  
103 rich in phyllosilicates. The ductile deformation, associated with peak meta-  
104 morphic conditions, is pervasive and apparent in (1) the foliation, defined  
105 both from the elongated shape of the blocks and the preferential orientation  
106 of the phyllosilicates in the matrix, (2) top-to-SE shear zones in the ma-  
107 trix and (3) stretching/necking of the blocks. At the grain scale, ductilely  
108 deformed quartz grains are preferentially elongated parallel to the foliation  
109 and show undulose extinction, subgrains and bulging grain boundaries (Fig.  
110 2A\_2). Note that the plastic deformation of quartz is more apparent in the  
111 west of the Hyuga *mélange* unit, in agreement with the slightly higher meta-  
112 morphic conditions, than along the eastern coast, which somehow explains  
113 why it is not described in Kondo et al. (2005).

114 The *mélange* rocks have been pervasively affected by quartz veining through-  
115 out their history. We define early-stage veins as those containing quartz  
116 grains that have been plastically deformed and late-stage veins as those cross-  
117 cutting the ductile deformation microstructures and containing grains devoid  
118 of plastic deformation. The latter veins are preferentially orientated perpen-  
119 dicular to the foliation and are often restricted to the blocks of the *mélange*,  
120 i.e. not propagating into the phyllosilicate-rich matrix.

121 All the quartz grains in veins contain fluid inclusions, most often with  
122 a very high density (Fig. 2). As plastic deformation of host quartz grains  
123 can potentially affect their volume, fluid inclusions predating or synchronous  
124 with the ductile phase cannot be studied by microthermometric methods,  
125 which assume an isochoric evolution of the inclusions from their trapping.  
126 Our study is thus necessarily restricted to late-stage quartz veins, devoid of  
127 plastic deformation (Fig. 2A and B).

128 In the Hyuga *mélange* (Fig. 1), Kondo et al. (2005) described two kinds of  
129 fluid inclusions in quartz veins: aqueous inclusions and gaseous CH<sub>4</sub>-bearing  
130 inclusions (Fig. 3). Assuming that these inclusions were cogenetic, Kondo  
131 et al. (2005) could derive the minimum  $P_t$  and  $T_t$  conditions of trapping from  
132 the intersection of the isochore of CH<sub>4</sub> inclusions with the  $T_{h, aq}$  isotherm (e.g.  
133 Mullis, 1979).

134 Our own analysis (microthermometry and Raman microspectrometry) of  
135 samples of Kondo et al. (2005) confirmed the presence of aqueous and gaseous  
136 CH<sub>4</sub>-rich inclusions. All these inclusions, distributed within late-stage veins,  
137 have very irregular shapes (Fig. 2A\_3 and B\_3). In some cases, they are  
138 clearly organized as planes of inclusions (Fig. 2B\_3), i.e. they are secondary  
139 inclusions; in other cases their nature is obscure. The cogenetic nature of  
140 these two kinds of inclusions, if possible, is questionable in two respects:

- 141 1. There is no textural evidence, apart from their presence in the same  
142 crystals, to the fact that water-rich and methane-rich fluid inclusions  
143 were trapped together and are thus representative of the two end-  
144 members of coexisting liquid and vapour fluid phases. In particular,  
145 the gaseous CH<sub>4</sub>-rich inclusions are all contained within fracture planes

146 that do not contain any aqueous inclusion. We found neither primary  
147 fluid inclusions of the two kinds in the same crystal or secondary inclu-  
148 sions of the two kinds in the same fracture plane.

149 2. Using a more extensive sampling of the Hyuga unit than Kondo et al.  
150 (2005), we discovered that gaseous CH<sub>4</sub>-rich inclusions are restricted,  
151 in fact, to the easternmost side, while water-rich fluid inclusions are  
152 distributed throughout the whole unit (blue dots in Fig. 1). Thus,  
153 the presence of CH<sub>4</sub>-rich inclusions appears rather as a peculiarity, and  
154 aqueous fluids are not necessarily considered to be at equilibrium with  
155 a CH<sub>4</sub>-rich phase and thus to represent the liquid aqueous end-member  
156 saturated with respect to a vapour CH<sub>4</sub>-rich phase.

157 As a consequence, these preliminary observations lead us to question the  
158 effective circulation of mixtures of methane-saturated waters and CH<sub>4</sub> gas  
159 during the trapping of fluid inclusions.

### 160 **3. Microthermometry**

#### 161 *3.1. Apparatus*

162 The selected quartz fragments were placed on a 200  $\mu\text{m}$ -thick, 1.6 cm-wide  
163 rounded glass window on top of the silver block of the THMS-600 Linkam  
164 heating-cooling stage. Phase changes in the inclusions were observed using an  
165 Olympus BHS microscope equipped with a  $\times 80$  ULWD Olympus objective  
166 and recorded by a Marlin black and white camera (CMOS 2/3" sensor, reso-  
167 lution  $1280 \times 1024$  pixels, pixel size of  $6.7 \mu\text{m}$ ). Temperature was measured  
168 using a class B Pt 100 thermistance, which has an intrinsic precision of  $0.15^\circ$   
169 to  $1.35^\circ\text{C}$  between  $0^\circ$  and  $600^\circ\text{C}$ . Temperature is sampled every  $\sim 300$  ms by

170 a Eurotherm 902 controller which allows analogic output. The temperature  
171 cycles of the stage (heating - cooling rate and temperature steps) are con-  
172 trolled using a LabVIEW® computer program. In the vicinity of the phase  
173 transitions, we chose slow heating rates about  $\sim 1^\circ\text{C}/\text{min}$ .

174 The stage was calibrated according to the procedure detailed in El Mekki-  
175 Azouzi (2010) between  $-56.6^\circ\text{C}$  and  $573^\circ\text{C}$  against 8 reference temperatures.

176 The standards used were:

- 177 1. either natural and synthetic fluid inclusions: melting point of  $\text{CO}_2$  at  
178  $-56.6^\circ\text{C}$ , melting point of ice :  $0^\circ\text{C}$ ,
- 179 2. or ceramics: solid - solid transitions at  $37^\circ\text{C}$  and  $47^\circ\text{C}$  in  $\text{CsPbCl}_3$  and  
180 at  $180^\circ\text{C}$  in  $\text{Pb}_3(\text{PO}_4)_2$ ,
- 181 3. or salts :  $b/g \rightarrow a$  transition at  $147^\circ\text{C}$  in  $\text{AgI}$  and subsequent melting  
182 at  $557^\circ\text{C}$ ,
- 183 4. or minerals :  $a \rightarrow b$  transition in quartz at  $573^\circ\text{C}$ .

184 Based on the calibration, the temperature accuracy is around  $\pm 1^\circ\text{C}$  over  
185 the whole investigation temperature range, from  $-120^\circ\text{C}$  to  $+290^\circ\text{C}$ , but much  
186 better, of the order of  $\pm 0.1^\circ\text{C}$  in the temperature range from  $-10^\circ$  to  $+20^\circ\text{C}$ ,  
187 where ice and gas hydrate melting occurs.

### 188 3.2. Gaseous methane-rich fluid inclusions

189 These inclusions are restricted to the easternmost, coastal side of the  
190 Hyuga unit. They are monophasic at ambient temperature. Upon cool-  
191 ing, they nucleate a bubble below  $-82.7^\circ\text{C}$  (the critical temperature of pure  
192 methane) and thus, we measured these homogenization temperatures ( $T_h$ ) to  
193 liquid.  $T_h$  distribution is roughly unimodal, with a principal peak between

194 -115°C and -105°C (Fig. 4), similar to what was described in Kondo et al.  
195 (2005).

### 196 3.3. Aqueous fluid inclusions

197 Water-rich fluid inclusions were collected in the whole Hyuga unit (Fig.  
198 1), including the eastern sides, where methane-rich inclusions are also present.  
199 At ambient temperature, they are biphasic, with a methane-rich bubble of  
200 vapor embedded in a water-rich liquid (Fig. 3). Upon heating, the size of  
201 the methane vapor bubble is progressively reduced, up to its complete dis-  
202 solution in the liquid phase at the homogenization temperature ( $T_{h,aq}$ ). In  
203 the final steps of heating, when the bubble has sufficiently shrunk, it is  
204 systematically affected by thermal agitation. The bubble rapid movement  
205 can be easily observed, even in very small (below 5  $\mu\text{m}$ ) inclusions, so that  
206  $T_{h,aq}$  estimation can be carried out efficiently on a large pool of inclusions of  
207 various size and shape. Homogenization temperatures are reproducible with  
208 a precision of  $\sim 1^\circ\text{C}$ . In the inclusions where all phase transitions were observ-  
209 able (Tab. 2),  $T_{h,aq}$  range from 200 to 280°C, i.e. similar to measurements  
210 by Kondo et al. (2005).

211 On the other hand, the measurements of the temperatures of ice melting  
212 ( $T_{mi}$ ) and gas hydrate disappearance ( $T_{hyd}$ ) are more difficult to carry out.  
213 In theory,  $T_{mi}$  and  $T_{hyd}$  can be estimated, during heating, by visual obser-  
214 vation of the disappearance of ice and gas hydrate, respectively. However,  
215 in practice, the inclusions are either too small or too crowded, so that the  
216 ice and and gas hydrate crystals are not visible. Fortunately, their presence,  
217 at the interface between the liquid and the vapor bubble, can be indirectly  
218 detected by their influence on the bubble shape, size or position within the

219 inclusion. As a consequence, we restricted the complete microthermometric  
220 observations to the largest fluid inclusions, and we had to apply a specific  
221 procedure of cyclic heating and cooling (Ramboz, 1980) to measure  $T_{mi}$  and  
222  $T_{hyd}$ .

223 The method of Ramboz (1980) is based on successive cycles of heating  
224 and cooling, which allow to determine the temperature of disappearance  
225 of ice/gas hydrate. It can be described as follows (Fig. 5 and movies in  
226 Supplementary Material):

- 227 1. First, freeze the inclusion up to formation of ice/gas hydrate.
- 228 2. Heat slowly the inclusion to melt progressively the ice/gas hydrate, up  
229 to a given temperature (let's say  $T_i$  for the cycle #i).
- 230 3. Then freeze very rapidly the inclusion and observe possible variations  
231 in its size, shape of location.
- 232 4. Repeat steps (2) and (3) for increasing  $T_i$  temperatures, until for some  
233  $T_n$ , rapid freezing has no effect on the vapour bubble (no shrinkage  
234 and no deformation). This indicates that ice/gas hydrate seeds have  
235 completely disappeared.

236 The melting temperature ( $T_m$ , i.e either  $T_{mi}$  or  $T_{hyd}$ ) of ice/gas hydrate  
237 is then approximated by  $T_{n-1} < T_m < T_n$ . The precision depends on the  
238 temperature increments, and it can be set up to the precision of the mi-  
239 crothermometric equipment (i.e. a precision of 0.1°C).

240 In practice, for ice, initial freezing was done at a temperature around  
241 -35 to -40°C (step 1), where ice filled instantaneously the inclusion. For  
242 gas hydrate, the temperature of initial freezing was above  $T_{mi}$ , i.e. at a state  
243 where the fluid inclusion contains three phases (gas hydrate, aqueous solution

244 and gas bubble).

245 For ice, the measurement of  $T_{mi}$  is systematically reproducible within  $\pm$   
246  $0.1^\circ\text{C}$ , as the bubble shrinkage caused by ice formation is easily detectable.  
247 However, for gas hydrates, the procedure is much less efficient. As the bulk  
248 content of  $\text{CH}_4$  is very low, the volumetric proportion of gas hydrate is also  
249 very low. Thus, its growth does not affect much the gas bubble, and its effect  
250 is only detectable in favourable cases, when the gas hydrate deforms the shape  
251 of the vapor bubble or changes its position in the inclusion. Hence, only a  
252 fraction of the inclusions showed some response to freezing/heating cycles.  
253 Moreover, in some of these inclusions, it was noted that the measurements  
254 of  $T_{\text{hyd}}$  were not reproducible after a complete freezing below  $\sim -40^\circ\text{C}$ . We  
255 postulate that the reason is a change in the position of the gas hydrate crystal  
256 seed, but had to discard the results of these inclusions.

257 Table 2 gives the complete data set ( $T_{mi}$ ,  $T_{\text{hyd}}$  and  $T_{h,\text{aq}}$ ) measured for  
258 seven aqueous inclusions. Homogenization temperatures  $T_{h,\text{aq}}$  range from  $\sim$   
259  $200^\circ$  to  $280^\circ\text{C}$ . On the other hand,  $T_{mi}$  and  $T_{\text{hyd}}$  are restricted to relatively  
260 narrow ranges, from  $-3.15^\circ$  to  $-1.9^\circ\text{C}$  and from  $5.3^\circ$  to  $10.4^\circ\text{C}$ , respectively.

#### 261 4. Thermodynamic modeling of aqueous inclusions

262 The fluid inclusions of this study can be ascribed to the  $\text{H}_2\text{O}-\text{CH}_4-\text{NaCl}$   
263 system. Thus, if they contain sufficient  $\text{CH}_4$ , they undergo the following  
264 phase transitions from low to high temperatures (Bakker, 1997; Bakker and  
265 Thiéry, 1994):

- 266 • first (state 1), melting of the last ice crystal in the presence of a gas  
267 hydrate (H), an aqueous solution ( $L_w$ ) and a gas bubble (G) at a tem-

268 perature  $T_1 = T_{mi}$ ,

- 269 • then (state 2), melting of the last gas hydrate crystal in the presence  
270 of an aqueous solution and a gas bubble at a temperature  $T_2 = T_{hyd}$ ,
- 271 • and eventually (state 3), disappearance of the gas bubble (homogeniza-  
272 tion point) at a temperature  $T_3 = T_{h,aq}$ .

273 To our knowledge, at least two thermodynamic models (Dubessy et al.,  
274 1992; Mao et al., 2011) have been devised to characterize such fluid inclu-  
275 sions exhibiting gas hydrates. However, none of them can be applied to the  
276 present study: the model of Dubessy et al. (1992) does not make use of  
277 homogenization temperatures and the model of Mao et al. (2011) does not  
278 allow for the presence of NaCl. Therefore, specific thermodynamic modeling  
279 has to be developed to interpret our microthermometric data. The method  
280 proposed here is an extension of the model of Dubessy et al. (1992), which  
281 has been associated to a  $\text{CH}_4$  solubility model (e.g. Duan and Mao, 2006) for  
282 NaCl-bearing aqueous solutions.

283 Our algorithm is based on the assumption that fluid inclusions behave as  
284 closed and isochoric systems. Thus, the key equations can be given by the  
285 following set of expressions:

$$\left\{ \begin{array}{l} n_{\text{H}_2\text{O},1} = n_{\text{H}_2\text{O},2} \\ n_{\text{CH}_4,1} = n_{\text{CH}_4,2} \\ n_{\text{NaCl},1} = n_{\text{NaCl},2} \\ \rho_2 = \rho_3 \end{array} \right. \quad (1)$$

286 where the meaning of the symbols used here (and in all what follows) is given  
287 in Table 1. The volume conservation between states 1 and 2, and between  
288 states 2 and 3, as well, is implicitly expressed in these equations. The first  
289 three equations express the mass balance of, respectively, H<sub>2</sub>O, CH<sub>4</sub> and  
290 NaCl, between state 1 (ice melting) and state 2 (gas hydrate melting) in a  
291 fluid inclusion of 1 m<sup>3</sup> of volume. The last equation formulates the mass  
292 conservation between state 2 and state 3 (homogenization).

293 As a consequence, this set of four equations represents a closed form of the  
294 constraints (volume and matter conservation) imposed on a fluid inclusion  
295 in the H<sub>2</sub>O-CH<sub>4</sub>-NaCl system. These equations are further developed in  
296 Appendix A. Other thermodynamic quantities do not explicitly appear in  
297 the equations above, but are implicitly required. In particular, this is the case  
298 of pressures of gas hydrate dissociation ( $P_1$  and  $P_2$ ), which are calculated by  
299 a thermodynamic model describing gas hydrate melting (e.g. Munck et al.,  
300 1988). NaCl activities in aqueous solutions are also needed and are calculated  
301 by a model for activity coefficients of dissolved salts (Pitzer, 1973). Molar  
302 volumes ( $V^G$ ) of the gas phase are calculated by the equation of state of  
303 Soave (1972). Additional details are given in Dubessy et al. (1992).

304 At the end, in the whole set of equations (1), it appears that there  
305 are only four unknowns:  $F_1^{Lw}$ , the volume proportion of the aqueous liquid  
306 at state 1;  $F_1^H$ , the volume proportion of gas hydrate at state 1;  $F_2^{Lw}$ , the  
307 volume proportion of aqueous solution at state 2; and  $m_{\text{NaCl},2}$ , the NaCl mo-  
308 lality in the aqueous solution at state 2. Thus, with four unknowns for four  
309 equations, the problem is completely solvable. Only one solution is found  
310 by using an iterative Newton algorithm for a given set of microthermometric

311 measurements ( $T_{mi}$ ,  $T_{hyd}$  and  $T_{h,aq}$ ). Therefore, the present procedure rep-  
312 resents an interesting enhancement of the method of Dubessy et al. (1992),  
313 which could not fully characterize the bulk properties of the fluid inclusion  
314 without relying upon the imprecise estimation of the bubble filling degree  
315  $F_2^G$  at  $T_2$ .

316 One discussion point is concerned with the error propagation produced by  
317 the successive equations of state used in our calculations. From the literature  
318 indications, the solubility models deviate at most by around 6% from exper-  
319 imental data (Duan and Mao, 2006; Spivey et al., 2004). Density models for  
320 H<sub>2</sub>O-NaCl solutions are more accurate with deviations within 1 % (Spivey  
321 et al., 2004; Duan and Mao, 2006). We have tested different combinations  
322 of thermodynamic models (Duan and Mao, 2006; Spivey et al., 2004; Duan  
323 et al., 1992; Potter and Brown, 1977; Pitzer, 1973) and we found no deviation  
324 above 12% in the calculated methane concentration, which is well consistent  
325 with the precision degree we estimated for our calculations.

## 326 **5. Reconstitution of paleo pressures and temperatures**

### 327 *5.1. P-T-X trapping conditions of the Hyuga mélange unit*

328 The thermodynamic modeling described in the preceding section has been  
329 applied to analyse the microthermometric data obtained on fluid inclusions  
330 from the Hyuga unit. Computed salinities and bulk methane concentrations  
331 are given in Table 2. Both show large relative variations, even within samples  
332 collected in the same area, either in the west (HN48, HN51 and HN87) or  
333 on eastern coast (Kon-NB26). CH<sub>4</sub> concentrations are positively correlated  
334 with homogenization temperatures, reflecting the fact that solubility at high

335  $P$  and  $T$  is mostly controlled by the temperature (Duan and Mao, 2006).  
336 Salinities are systematically below oceanic levels.

337 Monophasic isochores of gaseous inclusions, calculated from the web page  
338 <http://webbook.nist.gov/chemistry/fluid/> from the National Institute of Stan-  
339 dards and Technology using the equation of state by Setzmann and Wagner  
340 (1991) and biphasic liquid-gas isochores of aqueous inclusions, calculated us-  
341 ing Duan and Mao (2006), are plotted in Fig. 6. From this diagram, one  
342 important conclusion emerges: isochores of gaseous inclusions do not inter-  
343 sect biphasic isochores of aqueous inclusions. They run even at much higher  
344 pressures than homogenization pressures of aqueous inclusions. Thus, aque-  
345 ous and gaseous inclusions cannot be cogenetic.

346 As a consequence, the inclusions have registered, at least, two types of  
347 fluid circulations with marked composition differences: one involving dense  
348 aqueous solutions with some minor dissolved methane, and another one com-  
349 posed of light methane-rich gas. Methane pulses have probably occurred at  
350 larger pressures than aqueous solutions, but at this stage, other arguments  
351 must be searched to constrain further the trapping pressures and tempera-  
352 tures of these fluids.

353 The problem can be partially solved by considering the rock maximum  
354 temperature ( $T_{\max}$ ), as recorded by the vitrinite reflectance (Kondo et al.,  
355 2005) or the illite crystallinity (Hara and Kimura, 2008; Mukoyoshi et al.,  
356 2009). Here,  $T_{\max}$  is of the order of  $250\text{-}280^{\circ}\text{C} \pm 30^{\circ}\text{C}$ , i.e. a temperature  
357 range in line with the highest of  $T_{h,\text{aq}}$  values (Fig. 6 and Tab. 2).

358 It is always possible that circulating fluids were significantly hotter than  
359 the host rock, but were not abundant enough to influence the bulk rock tem-

360 perature (i.e.  $T_t > T_{\max}$ ). However, a large temperature discrepancy between  
 361  $T_t$  and  $T_{\max}$  is unlikely, as the rocks considered here are pervasively filled by  
 362 quartz veins, corresponding originally to circulating fluids. Furthermore, in  
 363 the case of a large  $T_t - T_{\max}$  disequilibrium, fluids would be trapped at various  
 364 temperatures ranging from  $T_{\max}$  (for small fluid pulses, locally buffered by the  
 365 bulk rock temperature) up to the fluid source temperature (for larger fluid  
 366 pulses, not buffered). Consequently, we should expect a broad distribution  
 367 for trapping temperatures  $T_t$  in this case.

368 However, Fig. 6 suggests a simpler solution. Indeed, it is striking that  
 369 the bulk rock peak temperatures ( $T_{\max}$ ) are roughly of the same magnitude  
 370 as:

- 371 1. either  $T_{h, \text{aq}}$  temperatures of aqueous inclusions (inclusions: Kon-NB26-  
 372 ech27 inclusion 26, HN51-4c, HN48b-inc a and inc b, HN87-inc c). In  
 373 this case,  $T_t = T_{h, \text{aq}}$  and  $P_t = P_{h, \text{aq}}$ . Most of the aqueous inclusions  
 374 have recorded these  $P_t - T_t$  conditions.
- 375 2. or temperatures of intersection points between monophasic isochores  
 376 of aqueous and gaseous inclusions (inclusions: Kon-NB26-ech27 inclu-  
 377 sions 27 and 30). In this case,  $T_t = T_{\max}$  and  $P_t = P_{\text{aq}}(T_t) = P_g(T_t)$   
 378 (where  $P_g$  is the pressure of gaseous inclusions along their monophasic  
 379 isochores). Both aqueous and gaseous inclusions have recorded these  
 380  $P_t - T_t$  conditions, but, as aqueous fluid inclusions are undersaturated  
 381 in methane (as they are in the single-phase domain, see Fig. 6), they  
 382 are not at equilibrium with gaseous inclusions. In other words, two  
 383 fluids penetrated the rock for these  $P$ - $T$  conditions, but they were not  
 384 at equilibrium with each other, hence not cogenetic. This case is an

385 illustration of the conditions to be fulfilled for two fluids to be at equi-  
386 librium, as developed in Ramboz et al. (1982): they must not only  
387 share the same  $P$  and  $T$  but also, in terms of composition, be exactly  
388 on the immiscibility surface between a methane-rich and a water-rich  
389 fluid. This latter condition can also be expressed as that the common  
390  $P$ - $T$  conditions must coincide with the saturation in methane for the  
391 aqueous inclusion.

392 In conclusion, we think that trapping occurred:

- 393 1. for roughly constant temperatures  $T_t \sim T_{\max}$  with fluids in thermal  
394 equilibrium with hosting rocks at temperatures between 250 and 280°C,
- 395 2. but in a retrometamorphic context featured by a large decrease in fluid  
396 pressure, from 250 to 50 MPa.

397 Furthermore, in both cases exposed above, aqueous fluids appear to be  
398 methane-undersaturated at their  $(P_t, T_t)$  trapping conditions, i.e. water-rich  
399 and methane-rich fluids, even when trapped for similar P-T conditions, are  
400 not at equilibrium with each other. Thus, during exhumation, we should not  
401 imagine the rock as being soaked by a single fluid mixture, but rather tran-  
402 siently percolated by pulses of higher-pressure, methane-rich fluids coming  
403 from the depth and in chemical disequilibrium with the local, lower-pressure  
404 aqueous fluid, undersaturated in methane.

## 405 5.2. *Geothermal evolution of the unit of the Hyuga melange unit*

406 The trapping conditions inferred in the preceding section correspond to  
407 a late-stage event in the polyphased history of the rocks, as aqueous and

408 gaseous inclusions are contained into late-stage veins that postdate the meta-  
409 morphic assemblages formed at peak conditions. When comparing the P-T  
410 evolution from the metamorphic peak to this late-stage event, pressure de-  
411 creased from 300-500 MPa, while temperature remained in the same range  
412 (Toriumi and Teruya, 1988), in other words, Hyuga unit was exhumed along  
413 a nearly isothermal path (Fig. 6). This exhumation pattern involves a sharp  
414 change in the thermal regime, from a geothermal gradient, for peak condi-  
415 tions, similar to the current subduction margin of SW Japan (Oleskevich  
416 et al., 1999; Hyndman et al., 1995; Peacock, 2009) to a much higher gradient  
417 during its late-stage evolution.

418 To estimate precisely this late-stage geothermal gradient from fluid in-  
419 clusion data, one needs to know where the fluid pressure is placed between  
420 hydrostatic and lithostatic pressure. Assuming hydrostatic fluid pressure  
421 yields a lower bound on the gradient; taking sedimentary rock volumic mass  
422 as  $2.7 \text{ g/cm}^3$ , the lowest fluid pressure recorded by aqueous fluid inclusions,  
423 50 MPa (Fig. 6), converts into a lithostatic pressure of 135 MPa, for a  
424 temperature of  $\sim 250^\circ\text{C}$ . This gradient is even higher than in the Cascadia  
425 subduction zone, the "hottest" modern margin for which thermal models are  
426 available (Oleskevich et al., 1999; Peacock, 2009).

427 The reasons for this thermal event are not yet clear. Terranes of the  
428 Shimanto Belt on Shikoku also recorded an event of late-stage heating, with  
429 water-rich associated fluids (Sakaguchi, 1996, 1999a,b), interpreted by these  
430 authors as the result of the subduction of a paleo-ridge at Eocene time (e.g.  
431 Lewis et al. (2000)). In Hyuga *mélange*, the youngest stratigraphic ages of  
432 blocks embedded in the matrix are Early Oligocene (Sakai et al., 1984). The

433 thermal event, which postdates the metamorphic deformation of these rocks,  
434 must therefore be significantly younger than Early Oligocene, hence cannot  
435 be explained by the Eocene paleo-ridge subduction. Another candidate is  
436 the subduction of the Shikoku Basin spreading center, on the Philippines sea  
437 plate, which was active from Early to Middle Miocene and which subducted  
438 nearly perpendicular to the margin (Letouzey and Kimura, 1985; Hall, 2002).  
439 As a result, the geothermal gradient in Middle Miocene, resulting from the  
440 subduction of an active ridge, was much higher than the modern one or  
441 the one that prevailed during the metamorphic deformation of the Hyuga  
442 *mélange*. Thermal models for the subduction along the SW Japan of a 15  
443 (i.e. the actual margin), 10 and 5 Ma old crust by Hyndman et al. (1995),  
444 give for the latter, young and hot oceanic crust, results in relative agreement  
445 with the late-stage gradient recorded by the aqueous fluid inclusions. One  
446 can also note that the Middle Miocene corresponds to a stage of widespread  
447 magmatism, as evidenced by numerous granite and granodiorite intrusions  
448 along the margin (Fig. 1), which may have further contributed to heat the  
449 deep rocks of the Shimanto accretionary prism. Although precise radiomet-  
450 ric dating are not yet available, we tentatively attribute the heating event  
451 recorded by the late-stage, aqueous inclusions analyzed here to the Middle  
452 Miocene tectonic and paleogeographic settings.

### 453 *5.3. A sensitive tool for pressure estimations in accretionary prisms*

454 To assess the  $P$ - $T$  conditions of fluid circulating at depth, fluid inclusions  
455 have been exploited in previous studies in accretionary prisms, like Kodiak  
456 in Alaska (Vrolijk, 1987; Vrolijk et al., 1988) or Shimanto in Japan (Lewis  
457 et al., 2000; Sakaguchi, 1999a; Kondo et al., 2005). These studies assume that

458 aqueous H<sub>2</sub>O-CH<sub>4</sub>-NaCl inclusions and gaseous CH<sub>4</sub> inclusions are cogenetic.  
459 This hypothesis is attractive as it allows to get a first approximate of the  
460 trapping  $P_t$ - $T_t$  conditions. However, in practice, the coevality of these fluid  
461 inclusions is extremely difficult to ascertain in rocks affected by multiple  
462 stages of deformation. Thus, the assumption of cogenetic trapping is no  
463 more satisfactory. The procedure we proposed here overcomes the problem  
464 and permits to get an independent estimation of trapping pressures  $P_t$  of  
465 aqueous H<sub>2</sub>O-CH<sub>4</sub>-NaCl inclusions. Additionally, this method is applicable  
466 even in the absence of CH<sub>4</sub> inclusions, as it is often the case in the Hyuga  
467 melange unit of the Shimanto Belt in Kyushu. And finally, this procedure  
468 is quite sensitive to small variations of bulk methane contents and trapping  
469 pressures.

470 To illustrate this point, let's consider the water-rich inclusions described  
471 in Vrolijk (1987) and Lewis et al. (2000), whose trapping conditions were  
472 determined as  $T \sim 260$ - $290^\circ\text{C}$  and  $P \sim 175$ - $300$  MPa and  $210$ - $250^\circ\text{C}$  and  $80$ -  
473  $100$  MPa, respectively. These two examples give an idea of the  $P$ - $T$  range  
474 of trapping conditions, with a relatively narrow range in temperature and a  
475 much larger range in pressure. Using our thermodynamic modeling, we have  
476 performed simulations for two inclusions in the system H<sub>2</sub>O-CH<sub>4</sub> with the  
477 same homogenization temperature  $T_{h, \text{aq}} = 250^\circ\text{C}$  and a gas hydrate melting  
478 temperature of  $9^\circ\text{C}$  and  $19^\circ\text{C}$ , respectively (Fig. 7 and Table 3, inclusions a  
479 and b). For  $T > T_{\text{hyd}}$ , inclusions are constituted of two phases, liquid and va-  
480 por, and evolve along an isochore up to  $T_{h, \text{aq}}$ , where the last bubble of vapor  
481 disappears. The two inclusions show a much different isochoric evolution up  
482 to  $T_{h, \text{aq}}$ , with a very large pressure increase for inclusion b, up to  $P_{h, \text{aq}} = 215$

483 MPa, and a much smaller pressure increase for the inclusion a, up to  $P_{h,aq}=48$   
484 MPa. The strong contrast between the two inclusions is primarily controlled  
485 by the very steep slope of the melting gas hydrate curve. A small increment  
486 in  $T_{hyd}$  results in a relatively large increase in the inclusion pressure, hence  
487 in the density of the methane in the bubble at temperature near ambient  
488 conditions: in inclusion a,  $P_{hyd}$  is 3 times larger than in inclusion b (Table  
489 3). As a result, bulk concentration of methane is larger, so that the pres-  
490 sure conditions required to dissolve completely the methane in the water, i.e.  
491  $P_{h,aq}$ , are much higher. One can note that the influence of  $T_{hyd}$  on methane  
492 concentration is dominant over volumic fraction: Inclusion a is less concen-  
493 trated in methane though the volumic fraction of methane bubble at ambient  
494 T is larger than inclusion b. The conclusion of this fictive example is that  
495 even a small quantity of methane in the inclusion strongly affects the P-V-T  
496 properties of the inclusions and raises their isochoric evolution towards high  
497 pressure. Therefore, in accretionary prisms (e.g. Vrolijk (1987); Sakaguchi  
498 (1999a)) or collision zones (e.g. Mullis (1979)) where dissolved methane is  
499 present in water, the estimation of realistic fluid pressure conditions requires  
500 to model the fluid in the ternary system  $H_2O-CH_4-NaCl$ . In other words,  
501 considering the fluid only in the simplified  $H_2O-NaCl$  system, whose liquid-  
502 vapor equilibrium curve runs at very low pressure, leads to underestimating  
503 the fluid pressure. Our new approach, which solves this systematic bias and  
504 can be used even for very low concentrations in methane, calls for a reap-  
505 praisal of cases, such as the high-pressure metamorphic stage recorded in the  
506 Schistes Lustrés in the Alps (Agard et al., 2000), where a large gap between  
507 fluid and mineral pressure was observed.

508 **6. Conclusion**

509 Fluid inclusions contained in rocks deformed in accretionary prisms or in  
510 orogenic contexts are the only key to unravel the composition, temperature  
511 and pressure of the fluids circulating at depth.

512 In this work, we have developed a new procedure to study methane-  
513 bearing aqueous inclusions, commonly found in such geodynamical contexts.  
514 The method depends only on microthermometric data, i.e.: the melting  
515 temperature of ice,  $T_{mi}$  the melting temperature of gas hydrate,  $T_{hyd}$  and  
516 the homogenization temperature,  $T_{h,aq}$ . It completely describes the physico-  
517 chemical properties of the aqueous inclusions (bulk density, composition,  
518 phase diagram) and  $P - T - composition$  of the circulating fluids. This  
519 method is based on an integrated algorithm, involving several state-of-the-  
520 art thermodynamic models for the  $H_2O-CH_4-NaCl$  system (solubility and  
521 density calculations, phase equilibria modeling) and has a relative precision  
522 within 10 %.

523 Modeling methane-bearing aqueous inclusions in the system  $H_2O-CH_4-$   
524  $NaCl$ , and not in the simplified  $H_2O-NaCl$  system, is necessary to reconstruct  
525 reliable fluid pressures in the depths of accretionary prisms or orogens. Fur-  
526 thermore, in cases where gaseous  $CH_4$  inclusions are present in addition to  
527 aqueous ones, our method enables to discuss the cogenetic character of the  
528 two kinds of inclusions, without invoking any textural argument, often ques-  
529 tionable in strongly deformed rocks.

530 We have applied this new method to the case study of the Hyuga unit  
531 from the Shimanto Belt (Japan). After careful microthermometric measure-  
532 ments, we show that aqueous and gaseous inclusions cannot be cogenetic,

533 in other words two fluids (a water-rich and a methane-rich one), in disequi-  
534 librium, were trapped in the rock at depth.  $P - T$  conditions recorded by  
535 aqueous inclusions show that after a nearly isothermal exhumation, a very  
536 hot geothermal gradient prevailed during the latest stage of the Hyuga unit  
537 evolution.

### 538 **Acknowledgment**

539 We thanks both reviewers and editor for their detailed and constructive  
540 reviews. This work has benefited from the financial support from the ANR  
541 programs SLABFLUX (K. Koga), CONGÉ (L. Mercury), INSU program  
542 SYSTER and ERC grant RHEOLITH (H. Raimbourg). The thermodynamic  
543 modeling has been carried out with a calculation software, which is freely  
544 available at [http://wwwobs.univ-bpclermont.fr/lmv/pperm/thierry\\_r/index.php](http://wwwobs.univ-bpclermont.fr/lmv/pperm/thierry_r/index.php).  
545 Raman spectrometry was done at the Thermodynamics Laboratory of the  
546 Blaise Pascal University (Clermont-Ferrand).

### 547 **Appendix A. Detailed equations**

548 Detailed equations, which are given below, are involved in the formulation  
549 of mass balance and volume conservation (equation (1)). For the sake of  
550 simplicity, it is understood that these equations are expressed for a fluid  
551 inclusion having a volume of  $1 \text{ m}^3$ .

#### 552 *Appendix A.1. State 1: ice melting*

553 First, when the last piece of ice disappears (state 1) at  $T_1 = T_{mi}$ , one has:

554

- the number moles of CH<sub>4</sub> and H<sub>2</sub>O in the gas:

$$\begin{cases} n_{\text{H}_2\text{O},1}^G = \frac{x_{\text{H}_2\text{O},1}^G (1 - F_1^{Lw} - F_1^H)}{V_1^G} \\ n_{\text{CH}_4,1}^G = \frac{(1 - x_{\text{H}_2\text{O},1}^G) (1 - F_1^{Lw} - F_1^H)}{V_1^G} \end{cases} \quad (\text{A.1})$$

555

- the number of moles of CH<sub>4</sub> and H<sub>2</sub>O in the gas hydrate:

$$\begin{cases} n_{\text{H}_2\text{O},1}^H = \frac{F_1^H \rho_1^H x_{\text{H}_2\text{O},1}^H}{M_{\text{CH}_4} x_{\text{CH}_4,1}^H + M_{\text{H}_2\text{O}} x_{\text{H}_2\text{O},1}^H} \\ n_{\text{CH}_4,1}^H = \frac{F_1^H \rho_1^H x_{\text{CH}_4,1}^H}{M_{\text{CH}_4} x_{\text{CH}_4,1}^H + M_{\text{H}_2\text{O}} x_{\text{H}_2\text{O},1}^H} \end{cases} \quad (\text{A.2})$$

556

- and the number of moles of H<sub>2</sub>O, CH<sub>4</sub> and NaCl in the aqueous solution:

$$\begin{cases} n_{\text{H}_2\text{O},1}^{Lw} = \frac{F_1^{Lw} \rho_1^{Lw}}{M_{\text{H}_2\text{O}} (1 + M_{\text{CH}_4} m_{\text{CH}_4,1} + M_{\text{NaCl}} m_{\text{NaCl},1})} \\ n_{\text{CH}_4,1}^{Lw} = \frac{F_1^{Lw} \rho_1^{Lw} m_{\text{CH}_4,1}}{1 + M_{\text{CH}_4} m_{\text{CH}_4,1} + M_{\text{NaCl}} m_{\text{NaCl},1}} \\ n_{\text{NaCl},1}^{Lw} = \frac{F_1^{Lw} \rho_1^{Lw} m_{\text{NaCl},1}}{1 + M_{\text{CH}_4} m_{\text{CH}_4,1} + M_{\text{NaCl}} m_{\text{NaCl},1}} \end{cases} \quad (\text{A.3})$$

557

The mole numbers of H<sub>2</sub>O, CH<sub>4</sub> and NaCl is then obtained from:

$$\begin{cases} n_{\text{CH}_4,1} = n_{\text{CH}_4,1}^G + n_{\text{CH}_4,1}^{Lw} + n_{\text{CH}_4,1}^H \\ n_{\text{H}_2\text{O},1} = n_{\text{H}_2\text{O},1}^G + n_{\text{H}_2\text{O},1}^{Lw} + n_{\text{H}_2\text{O},1}^H \\ n_{\text{NaCl},1} = n_{\text{NaCl},1}^{Lw} \end{cases} \quad (\text{A.4})$$

558

where different quantities are yielded by equations A.1, A.2 and A.3.

559 *Appendix A.2. State 2: gas hydrate melting*

560 In the same way, similar equations are derived for state 2 (i.e. when the  
561 last nugget of gas hydrate melts at  $T_2 = T_{\text{hyd}}$ ):

- 562 • the number of moles of  $\text{H}_2\text{O}$  and  $\text{CH}_4$  in the gas:

$$\begin{cases} n_{\text{H}_2\text{O},2}^G = \frac{x_{\text{H}_2\text{O},2}^G (1 - F_2^{Lw})}{V_2^G} \\ n_{\text{CH}_4,2}^G = \frac{x_{\text{CH}_4,2}^G (1 - F_2^{Lw})}{V_2^G} \end{cases} \quad (\text{A.5})$$

- 563 • the number of moles of  $\text{H}_2\text{O}$ ,  $\text{CH}_4$  and  $\text{NaCl}$  in the aqueous phase:

$$\begin{cases} n_{\text{H}_2\text{O},2}^{Lw} = \frac{F_2^{Lw} \rho_2^{Lw}}{M_{\text{H}_2\text{O}} (1 + M_{\text{CH}_4} m_{\text{CH}_4,2} + M_{\text{NaCl}} m_{\text{NaCl},2})} \\ n_{\text{CH}_4,2}^{Lw} = \frac{F_2^{Lw} \rho_2^{Lw} m_{\text{CH}_4,2}}{1 + M_{\text{CH}_4} m_{\text{CH}_4,2} + M_{\text{NaCl}} m_{\text{NaCl},2}} \\ n_{\text{NaCl},2}^{Lw} = \frac{F_2^{Lw} \rho_2^{Lw} m_{\text{NaCl},2}}{1 + M_{\text{CH}_4} m_{\text{CH}_4,2} + M_{\text{NaCl}} m_{\text{NaCl},2}} \end{cases} \quad (\text{A.6})$$

- 564 • the total number of moles of  $\text{H}_2\text{O}$ ,  $\text{CH}_4$  and  $\text{NaCl}$  in a volume of  $1 \text{ m}^3$ :

$$\begin{cases} n_{\text{H}_2\text{O},2} = n_{\text{H}_2\text{O},2}^G + n_{\text{H}_2\text{O},2}^{Lw} \\ n_{\text{CH}_4,2} = n_{\text{CH}_4,2}^G + n_{\text{CH}_4,2}^{Lw} \\ n_{\text{NaCl},2} = n_{\text{NaCl},2}^{Lw} \end{cases} \quad (\text{A.7})$$

565 where right-hand terms are calculated by equations A.5 and A.6.

566 *Appendix A.3. Bulk volume conservation*

567 And finally, the bulk densities of the fluid inclusion at states 2 and 3, are  
568 given respectively by:

$$\begin{cases} \rho_2 = F_2^{L_w} \rho_2^{L_w} + (1 - F_2^{L_w}) \frac{M_{\text{CH}_4} x_{\text{CH}_4,2}^G + M_{\text{H}_2\text{O}} x_{\text{H}_2\text{O},2}^G}{V_2^G} \\ \rho_3 = \rho_3^{L_w} \end{cases} \quad (\text{A.8})$$

569 where densities  $\rho_2^{L_w}$  and  $\rho_3^{L_w}$  of the aqueous solution are obtained from:

$$\begin{cases} \rho_2^{L_w} = \frac{1 + M_{\text{CH}_4} m_{\text{CH}_4,2} + M_{\text{NaCl}} m_{\text{NaCl},2}}{1/\rho_2^* + m_{\text{CH}_4,2} v_{\text{CH}_4}} \\ \rho_3^{L_w} = \frac{1 + M_{\text{CH}_4} m_{\text{CH}_4,3} + M_{\text{NaCl}} m_{\text{NaCl},3}}{1/\rho_3^* + m_{\text{CH}_4,3} v_{\text{CH}_4}} \end{cases} \quad (\text{A.9})$$

570 where  $\rho^*$  is the density (kg/m<sup>3</sup>) of the H<sub>2</sub>O-NaCl aqueous solution for  $T$ ,  
 571  $P$  and  $m_{\text{NaCl}}$  conditions, and  $v_{\text{CH}_4}$  is the partial molar volume (m<sup>3</sup>/mol) of  
 572 dissolved CH<sub>4</sub> calculated by a solubility model (e.g. Duan et al., 1992).

## 573 References

- 574 Agard, P., Goffé, P., Touret, J.L.R., Vidal, O., 2000. Retrograde mineral and  
 575 fluid evolution on high-pressure metapelites (Schistes lustrés unit, Western  
 576 Alps). *Contrib. Mineral. Petrol.* 140, 296–315.
- 577 Alderton, D., Bevins, R., 1996.  $P$ – $T$  conditions in the South Wales Coalfield:  
 578 evidence from coexisting hydrocarbon and aqueous fluid inclusions. *J.*  
 579 *Geol. Soc. London* 153, 265–275.
- 580 Bakker, R., 1997. Clathrates: Computer programs to calculate fluid inclu-  
 581 sion v-x properties using clathrate melting temperature. *Computers &*  
 582 *Geosciences*, 1–18.
- 583 Bakker, R., Thiéry, R., 1994. Application of clathrates to fluid inclusion  
 584 studies, in: De Vivo, B., Frezzotti, M. (Eds.), *Fluid inclusions in minerals:*  
 585 *methods and applications.*, Virginia Tech, Blacksburg, USA. pp. 191–208.

- 586 Berman, R., 1991. Thermobarometry using multi-equilibrium calculation: a  
587 new technique, with petrological applications. *The Canadian Mineralogist*  
588 29, 833–855.
- 589 Dalla Torre, M., DeCapitani, C., Frey, M., Underwood, M., Mullis, J., Cox,  
590 R., 1996. Very low-temperature metamorphism of shales from the Diablo  
591 Range, Franciscan Complex, California: New constraints on the exhuma-  
592 tion path. *GSA. Bull.* 108, 578–601.
- 593 Duan, Z., Mao, S., 2006. A thermodynamic model for calculating methane  
594 solubility, density and gas phase composition of methane-bearing aqueous  
595 fluids from 273 to 523K and 1 to 2000 bars. *Geochim. Cosmochim. Acta*  
596 70, 3369–3386.
- 597 Duan, Z., Moller, N., Greenberg, J., Weare, J., 1992. The prediction of  
598 methane solubility in natural waters to high ionic strength from 0 to 250 °C  
599 and from 0 to 1600 bar. *Geochim. Cosmochim. Acta* 56, 1451–1460.
- 600 Dubessy, J., Thiéry, R., Canals, M., 1992. Modelling of phase equilibria  
601 involving mixed gas clathrates: Application to the determination of molar  
602 volume of the vapour phase and salinity of the aqueous solution in fluid  
603 inclusions. *Eur. J. Mineral.* 4, 873–884.
- 604 El Mekki-Azouzi, M., 2010. Etude expérimentale de l'eau et des solutions  
605 aqueuses métastables - implications pour le milieu naturel. Ph.D. thesis.  
606 ISTO. Université d'Orléans. Orléans.
- 607 Hall, R., 2002. Cenozoic geological and plate tectonic evolution of SE Asia

- 608 and the SW Pacific: Computer-based reconstruction, models and anima-  
609 tions. *J. Asian Earth Sci.* 20, 353–431.
- 610 Hara, H., Kimura, K., 2008. Metamorphic cooling history of the Shimanto  
611 accretionary complex, Kyushu, southwest Japan: Implications for the tim-  
612 ing of out-of-sequence thrusting. *Island Arc* 17, 546–559.
- 613 Hyndman, R., Wang, K., Yamano, M., 1995. Thermal constraints on the seis-  
614 mogenic portion of the southwestern Japan subduction thrust. *J. Geophys.*  
615 *Res.* 100, 15,373–15,392.
- 616 Imai, I., Teraoka, Y., Okumura, K., 1971. Geologic structure and metamor-  
617 phic zonation of the northeastern part of the Shimanto terrane in Kyushu,  
618 Japan. *J. Geol. Soc. Jap.* 77, 207–220.
- 619 Kondo, H., Kimura, G., Masago, H., Ohmori-Ikehara, K., Kitamura, Y., Ike-  
620 sawa, E., Sakaguchi, A., Yamaguchi, A., Okamoto, S., 2005. Deformation  
621 and fluid flow of a major out-of-sequence thrust located at seismogenic  
622 depth in an accretionary complex: Nobeoka Thrust in the Shimanto Belt,  
623 Kyushu, Japan. *Tectonics* 24, 1–16.
- 624 Letouzey, J., Kimura, M., 1985. Okinawa trough genesis: Structure and  
625 evolution of a backarc basin developed in a continent. *Mar. Petrol. Geol.*  
626 2, 111–130.
- 627 Lewis, J., Byrne, T., Pasteris, J., London, D., Morgan VI, G., 2000. Early  
628 Tertiary fluid flow and pressure–temperature conditions in the Shimanto  
629 accretionary complex of southwest Japan: constraints from fluid inclusions.  
630 *J. Metamorphic Geol.* 18, 319–333.

- 631 Lin, F., Sum, A., Bodnar, R., 2007. Correlation of methane raman  $\nu_1$  band  
632 position with fluid density and interactions at the molecular level. *J. Ra-*  
633 *man Spectrosc.* 38, 1510–1515.
- 634 Mao, S., Duan, Z., Zhang, D., Shi, L., Chen, Y., Li, J., 2011. Thermodynamic  
635 modeling of binary  $\text{CH}_4\text{-H}_2\text{O}$  fluid inclusions. *Geochim. Cosmochim. Ac.*  
636 75, 5892–5902.
- 637 Mukoyoshi, H., Hirono, T., Hara, H., Sekine, K., Tsuchiya, N., Sakaguchi,  
638 A., Soh, W., 2009. Style of fluid flow and deformation in and around an  
639 ancient out-of-sequence thrust: An example from the Nobeoka tectonic  
640 line in the Shimanto accretionary complex, southwest Japan. *Island Arc*  
641 18, 333–351.
- 642 Mullis, J., 1979. The system methane-water as a geological thermometer and  
643 barometer from the external part of the Central Alps. *Bull. Mineral.* 102,  
644 526–536.
- 645 Mullis, J., Dubessy, J., Poty, B., O’Neil, J., 1994. Fluid regimes during late  
646 stages of a continental collision: Physical, chemical, and stable isotope  
647 measurements of fluid inclusions in fissure quartz from a geotraverse in the  
648 Central Alps, Switzerland. *Geochim. Cosmochim. Ac.* 58, 2239–2267.
- 649 Munck, J., Skold-Jorgensen, S., Rasmussen, P., 1988. Computation of for-  
650 mation of gas hydrates. *Chem. Eng. Sci.* 43, 2661–2672.
- 651 Murata, A., 1997. Geological map of Miyazaki prefecture (1:200,000).
- 652 Oleskevich, D., Hyndman, R., Wang, K., 1999. The updip and downdip  
653 limits to great subduction earthquakes: Thermal and structural models

- 654 of Cascadia, south Alaska, SW Japan and Chile. *J. Geophys. Res.* 104,  
655 14,965–14,991.
- 656 Peacock, S., 2009. Thermal and metamorphic environment of subduction  
657 zone episodic tremor and slip. *J. Geophys. Res.* 114, 1–9.
- 658 Pichavant, M., Ramboz, C., Weisbrod, A., 1982. Fluid immiscibility in nat-  
659 ural processes : use and misuse of fluid inclusion data. I. phase equilibria  
660 analysis-a theoretical and geometrical approach. *Chem. Geol.* 37, 1–27.
- 661 Pitzer, K., 1973. Thermodynamics of electrolytes. 1: Theoretical basis and  
662 general equations. *J. Phys. Chem.* 77, 268–277.
- 663 Potter, R., Brown, D., 1977. The volumetric properties of aqueous sodium  
664 chloride solutions from 0 °C to 500 °C at pressures up to 2000 bars based  
665 on a regression of available data in the literature. preliminary steam tables  
666 for NaCl solutions. *Geological Survey Bulletin* 1421-C, 1–45.
- 667 Powell, R., Holland, T., 1988. An internally consistent dataset with un-  
668 certainties and correlations: 3. applications to geobarometry, worked ex-  
669 amples and a computer program. *Journal of Metamorphic Geology* 6,  
670 173–204.
- 671 Ramboz, C., 1980. Problèmes posés par la détermination de la compo-  
672 sition de fluides carboniques complexes, à l'aide des techniques microther-  
673 mométriques. *C. R. Acad. Sc. Paris, serie D* 290, 499–502.
- 674 Ramboz, C., Pichavant, M., Weisbrod, A., 1982. Fluid immiscibility in nat-  
675 ural processes: Use and misuse of fluid inclusion data. ii. interpretation of  
676 fluid inclusion data in terms of immiscibility. *Chem. Geol.* 37, 29–48.

- 677 Sadofsky, S., Bebout, G.E., 2004. Field and isotopic evidence for fluid mo-  
678 bility in the Franciscan Complex: Forearc paleohydrology to depths of 30  
679 kilometers. *Int. Geol. Rev.* 46, 1053–1088.
- 680 Sakaguchi, A., 1996. High paleogeothermal gradient with ridge subduction  
681 beneath the Cretaceous Shimanto accretionary prism, southwest Japan.  
682 *Geology* 24, 795–798.
- 683 Sakaguchi, A., 1999a. Thermal maturity in the Shimanto accretionary prism,  
684 southwest Japan, with the thermal change of the subducting slab: Fluid  
685 inclusion and vitrinite reflectance study. *Earth Planet. Sci. Lett.* 173, 61–  
686 74.
- 687 Sakaguchi, A., 1999b. Thermal structure and paleo-heat flow in the Shimanto  
688 accretionary prism Shimanto accretionary prism. *The Island Arc* 8, 359–372.
- 689 Sakai, T., Nishi, H., Saito, T., Nakaseko, K., Nishimura, A., 1984. Microfossil  
690 stratigraphy of the paleogene system in kyushu shimanto belt, in: T., S.,  
691 Okada, H., Kaiho, K. (Eds.), *Biostratigraphy and international correlation*  
692 *of the Paleogene system in Japan*, Virginia Tech. pp. 95–112.
- 693 Setzmann, U., Wagner, W., 1991. A new equation of state and tables of  
694 thermodynamic properties for methane covering the range from the melting  
695 line to 625K at pressures up to 1000 MPa. *J. Phys. Chem. Ref. Data* 20,  
696 1061–1151.
- 697 Soave, G., 1972. Equilibrium constants from a modified Redlich-Kwong equa-  
698 tion of state. *Chem. Eng. Sci.* 27, 1197–1203.

- 699 Spivey, J., McCain, W., North, R., 2004. Estimating density, formation vol-  
700 ume factor, compressibility, methane solubility, and viscosity for oilfield  
701 brines at temperatures from 0 to 275 °C, pressures to 200 MPa, and salin-  
702 ities to 5.7 mole/kg. *J. Can. Petrol. Technol* 43, 52–60.
- 703 Taira, A., Katto, J., Tashiro, M., Okamura, M., Kodama, K., 1988. The  
704 Shimanto Belt in Shikoku, Japan—Evolution of Cretaceous to Miocene ac-  
705 cretionary prism. *Modern Geology* 12, 5–46.
- 706 Toriumi, M., Teruya, J., 1988. Tectono-metamorphism of the Shimanto Belt.  
707 *Modern Geology* 12, 303–324.
- 708 Vrolijk, P., 1987. Tectonically-driven fluid flow in the Kodiak accretionary  
709 complex, Alaska. *Geology* 15, 466–469.
- 710 Vrolijk, P., Myers, G., Moore, J., 1988. Warm fluid migration along tectonic  
711 melanges in the Kodiak accretionary complex, Alaska. *J. Geophys. Res.*  
712 93, 10,313–10,324.

## 713 **Tables**

Table 1: List of symbols

Table 2: Summary of data for seven representative aqueous inclusions from the Hyuga formation. Input data ( $T_{mi}$ ,  $T_{hyd}$  and  $T_{h, aq}$  temperatures obtained by microthermometry) permit to characterize the fluid inclusion at different states (in particular, homogenization point and gas hydrate melting point).

Table 3: P-V-T-composition properties of the two fictive inclusions described in 5.3 and in Fig. 7.

## 714 **Figures**

Figure 1: Simplified geological map of the Shimanto Belt on eastern Kyushu, Japan, from Murata (1997); Taira et al. (1988). The Nobeoka Tectonic Line (NTL) constitutes a major tectonic boundary between northern and southern Shimanto. All the samples studied here in microthermometry (red stars) were collected in the highly deformed Hyuga *mélange* unit, in the footwall of the NTL. Blue dots corresponds to other samples of the same unit, where two-phased, aqueous fluid inclusions are also present. Methane-rich inclusions could be found only near the easternmost extension of the NTL, i.e. near sample Kon-NB26.

Figure 2: Structures of quartz grains and included fluid inclusions. A: A early-stage vein of quartz, elongated parallel to the foliation, is crosscut by a late-stage vein, visible by its lower density in fluid inclusions. The quartz grains constituting the early-stage veins are elongated parallel to the foliation and show undulose extinction, subgrain formation and grain boundary bulging, while the late-stage vein is virtually undeformed. The late-stage vein contains aqueous fluid inclusions, two-phased at ambient temperature. These inclusions are aligned along fracture planes parallel to the vein walls and have themselves an elongated shape parallel to the same direction. B- Undeformed quartz vein showing a variable density of fluid inclusions. Note in picture 2 that a single quartz grain hosts domains of low and high density of inclusions. Fluid inclusions have the same composition and geometry as A. All pictures: optical microscope, A.2 and B.2 with crossed nicols.

Figure 3: Aqueous and gaseous inclusions were the two types of fluid inclusions, which could be easily identified by their very different microthermometric properties and Raman spectra at ambient temperatures. (A) aqueous inclusion, exhibiting a CH<sub>4</sub>-rich bubble immersed in an aqueous solution; (B) gaseous inclusion composed essentially by a CH<sub>4</sub> fluid; (C and D) normalized Raman spectra focused on different parts (x, y or z) of the inclusions pictured above. The broad peak of water between 3000 and 3800cm<sup>-1</sup> and the  $\nu_1$  sharp peak near 2918cm<sup>-1</sup> of the methane vapour are well visible (Lin et al., 2007).

Figure 4: Distribution of homogenization temperatures  $T_{h,aq}$  of gaseous inclusions in the sample NB25-#46-zoneB, collected near sample Kon-NB26 in Fig. 1.

Figure 5: Determination procedure of  $T_{mi}$  (a to d) and  $T_{hyd}$  (e to h). We start at low temperatures to nucleate ice (a) or gas hydrate (e). Then, we slowly heat up to some fixed temperature  $T_i$  (b and f) and we freeze rapidly the fluid inclusion (c and g). If the freezing triggers movement/deformation of the methane vapor bubble, this means that some ice (gas hydrate) was still present at  $T_i$ . Thus, we repeat a new heating/freezing cycle, but with a  $T_i$  incremented by 0.1 °C, until the freezing does not induce any detectable change of the bubble behaviour (d and h). The last  $T_i$  yields then a good approximation of the disappearance temperature of ice (or gas hydrate).

Figure 6:  $P$ - $T$  diagram illustrating the main results obtained from microthermometry and thermodynamic modeling. Black lines are monophasic isochores of gaseous  $\text{CH}_4$  inclusions, homogenizing mostly between  $-115$  and  $-95^\circ\text{C}$ . Blue lines are isochores calculated for the aqueous inclusions: solid curves represent biphasic liquid-gas isochores, whereas dashed lines are monophasic liquid isochores. Biphasic isochores start from gas hydrate melting points (filled diamonds) and end at homogenization points (empty diamonds). The shaded area represents the peak temperatures of host formation estimated from petrological analyses. The dark arrow symbolizes the earliest stage of isothermal exhumation of the formation, starting from peak metamorphic conditions (empty rectangle, from Toriumi and Teruya (1988)), down to the trapping conditions of aqueous fluid inclusions.

Figure 7:  $P$ - $T$  evolution of two fictive inclusions in the system  $\text{H}_2\text{O}$ - $\text{CH}_4$ , with the same  $T_{h,\text{aq}}=250^\circ\text{C}$  but contrasted  $T_{\text{hyd}}$ , either  $9^\circ\text{C}$  (a) or  $19^\circ\text{C}$  (b). Each inclusion is three-phased (liquid+vapour+gas hydrate) from  $T_{mi}$  to  $T_{\text{hyd}}$ , two-phased (liquid+vapour) from  $T_{\text{hyd}}$  to  $T_{h,\text{aq}}$ , then single-phased (vapour) for  $T > T_{h,\text{aq}}$ . Phase transitions occur along the gas hydrate melting curve and the methane solubility curve corresponding to methane concentration of each inclusion. From the comparison of the two inclusion, one can see that a small increase in gas hydrate melting temperature results in a large increase in pressure at homogenization.

715       Supplementary Material: Movies illustrating the cycling procedure to  
716 estimate precisely  $T_{mi}$  and  $T_{hyd}$ . Each cycle is composed of a slow heating  
717 phase, followed by rapid freezing. The presence/absence of a crystal of ice or  
718 gas hydrate at the maximum temperature  $T_i$  of each cycle is detected by the  
719 rapid crystal growth upon freezing, which triggers the shrinkage, movement  
720 or deformation of the gas bubble. Note that the temperature embedded in  
721 the movies needs a correction determined by calibrating the heating/freezing  
722 stage.

723       Movie 1: Cycle  $i$  to measure  $T_{mi}$ . As  $T$  is slowly increased up to  $T_i$ , the  
724 bubble expands. Rapid freezing results in bubble shrinkage, showing that ice  
725 was still present at  $T_i$ .

726       Movie 2: Cycle  $j$  to measure  $T_{mi}$ . As  $T$  is slowly increased up to  $T_j$ , the  
727 bubble expands. Rapid freezing has no effect on the bubble, showing that  
728 ice was no longer present at  $T_j$ .

729       Movie 3: Cycle  $i$  to measure  $T_{hyd}$ . As  $T$  is slowly increased up to  $T_i$ , the  
730 bubble moves and deforms. Rapid freezing results in the movement of the  
731 bubble towards the bottom of the picture, showing that gas hydrate was still  
732 present at  $T_i$ .

733       Movie 4: Cycle  $j$  to measure  $T_{hyd}$ . As  $T$  is slowly increased up to  $T_j$ ,  
734 the bubble moves and deforms. Rapid freezing has no effect on the bubble,  
735 showing that gas hydrate was no longer present at  $T_j$ .

Symbol	Signification
subscript $i$	component ( $i$ either H <sub>2</sub> O or CH <sub>4</sub> or NaCl )
superscript $j$	phase ( $j = H$ for gas hydrate; $j = L_w$ for aqueous solution; and $j = G$ for gas)
subscript $k$	state ( $k = 1$ for ice disappearance point; $k = 2$ for gas hydrate disappearance point; $k = 3$ for homogenization point)
$n_i$	bulk mole density of component $i$ (mol/m <sup>3</sup> )
$T$	temperature
$T_{mi}$	ice melting temperature
$T_{hyd}$	gas hydrate melting temperature
$T_{h,aq}$	homogenization temperature of aqueous inclusions
$T_h$	homogenization temperature
$T_t$	trapping temperature
$T_{max}$	rock maximum temperature
$P$	pressure
$P_t$	trapping pressure
$P_{h,aq}$	homogenization pressure of aqueous inclusions
$P_g$	pressure of a gaseous isochore along its monophasic isochore
$\rho$	bulk mass density of a fluid inclusion (kg/m <sup>3</sup> )
$\rho_k^j$	mass density of phase $j$ at state $k$
$\rho^*$	density of a H <sub>2</sub> O-NaCl aqueous solution
$n_i^j$	number of moles of component $i$ in phase $j$
$n_{i,k}^j$	number of moles of component $i$ in phase $j$

Sample	Kon-NB26-ech			27	HN51	HN48B		HN87
Inclusion	26	29	30	4c	inc a	inc b	inc c	
Data								
$T_{mi}$ (°C)	-3.15	-2.9	-2.3	-3	-1.9	-2	-1.9	
$T_{hyd}$ (°C)	9.5	8.7	8.5	10.25	6.7	5.3	10.4	
$T_{h,aq}$ (°C)	239	198	207	252	248	275	277	
State 3 (homogenization point)								
$P_{h,aq}$ (MPa)	80.9	80.3	69.9	83.0	44.7	35.3	64.1	
$\rho_3^{Lw}$ (kg/m <sup>3</sup> )	892	934	914	876	849	809	819	
$m_{CH_4,3}$ (mol/kg H <sub>2</sub> O)	0.85	0.53	0.57	1.02	0.70	0.76	1.26	
$m_{NaCl,3}$ (mol/kg H <sub>2</sub> O)	0.83	0.77	0.60	0.77	0.49	0.52	0.46	
State 2 (gas hydrate melting)								
$P_2$ (MPa)	8.6	7.8	7.3	9.2	5.8	5.1	8.6	
$F_2^G$ %	15	10	12	16	18	22	21	

Table 2:

Sample	a	b
Data		
$T_{mi}$ (°C)	0	0
$T_{hyd}$ (°C)	9	19
$T_{h, aq}$ (°C)	250	250
State 3 (homogenization point)		
$P_{h, aq}$ (MPa)	47.6	215.6
$\rho_3^{Lw}$ (kg/m <sup>3</sup> )	824	891
$m_{CH_4, 3}$ (mol/kg H <sub>2</sub> O)	0.83	1.72
$m_{NaCl, 3}$ (mol/kg H <sub>2</sub> O)	0	0
State 2 (gas hydrate melting)		
$P_2$ (MPa)	6.6	20.9
$F_2^G$ %	0.19	0.13

Table 3:

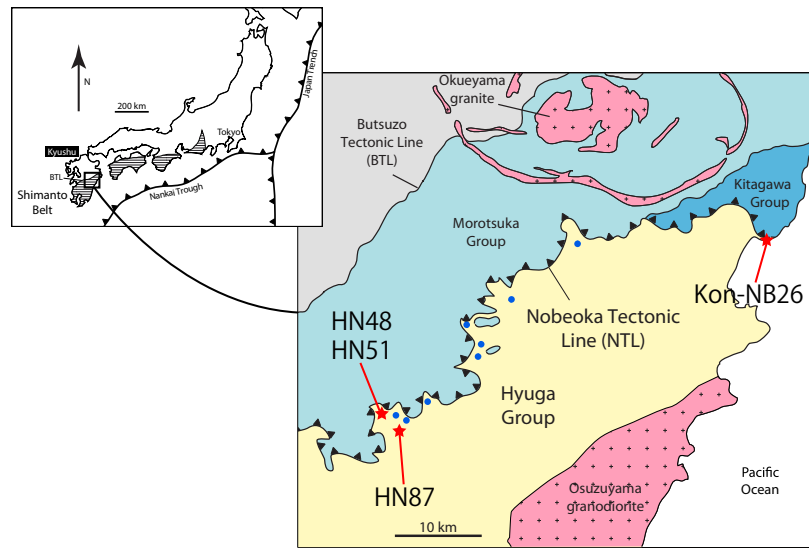


Figure 1:

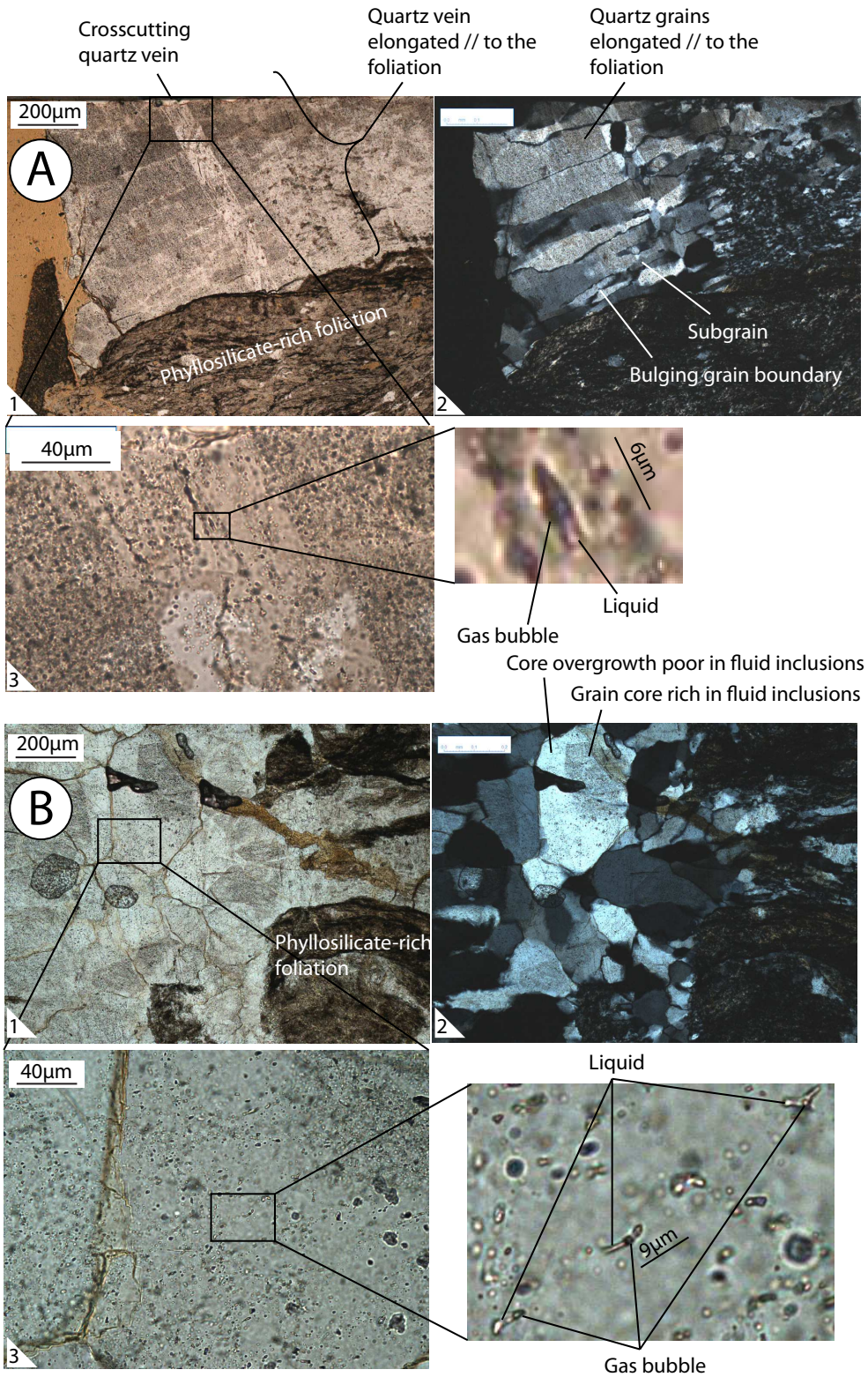


Figure 2:

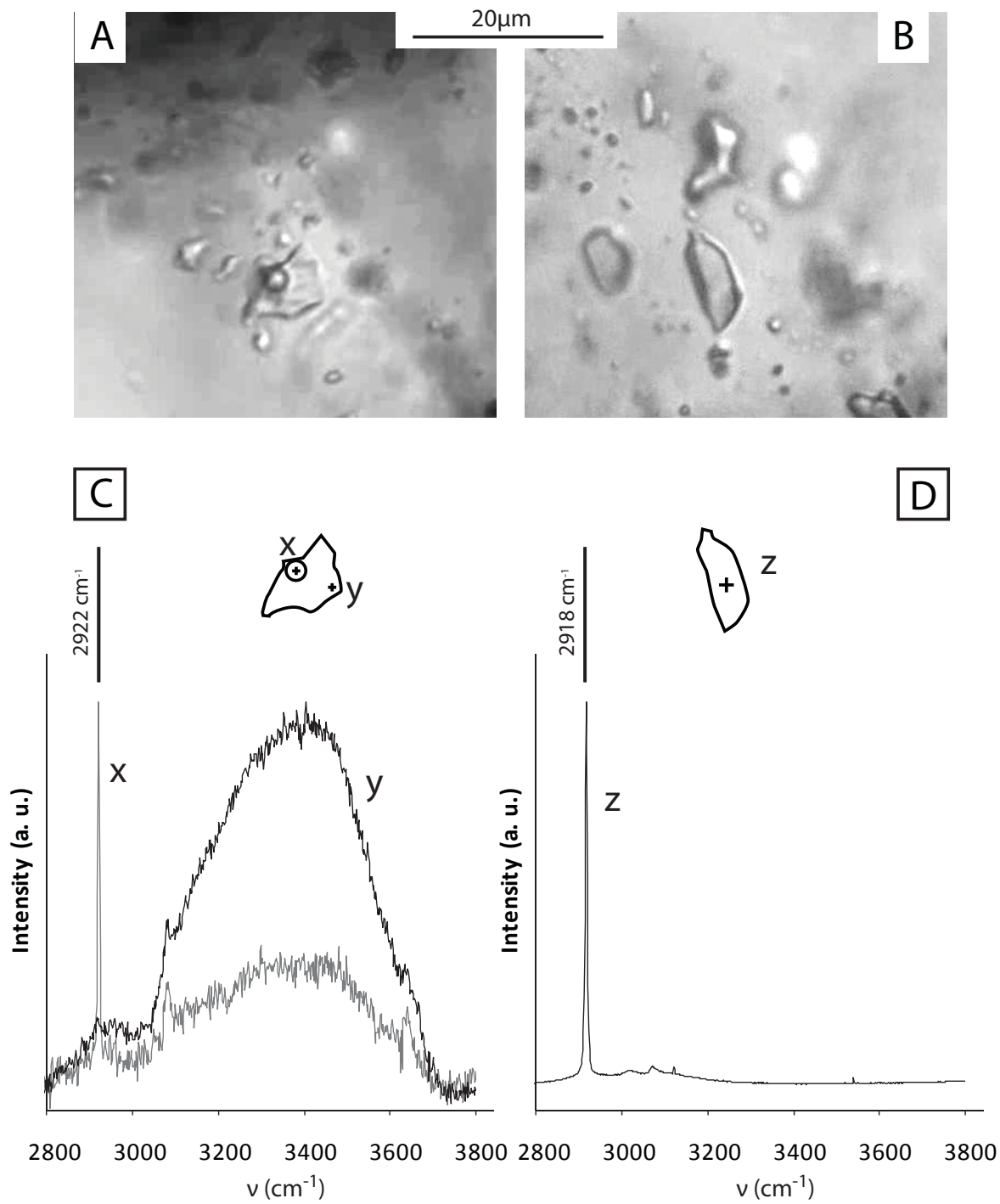


Figure 3:

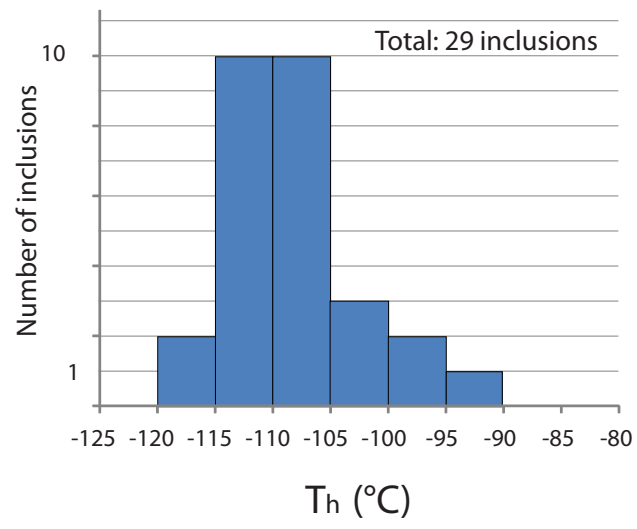


Figure 4:

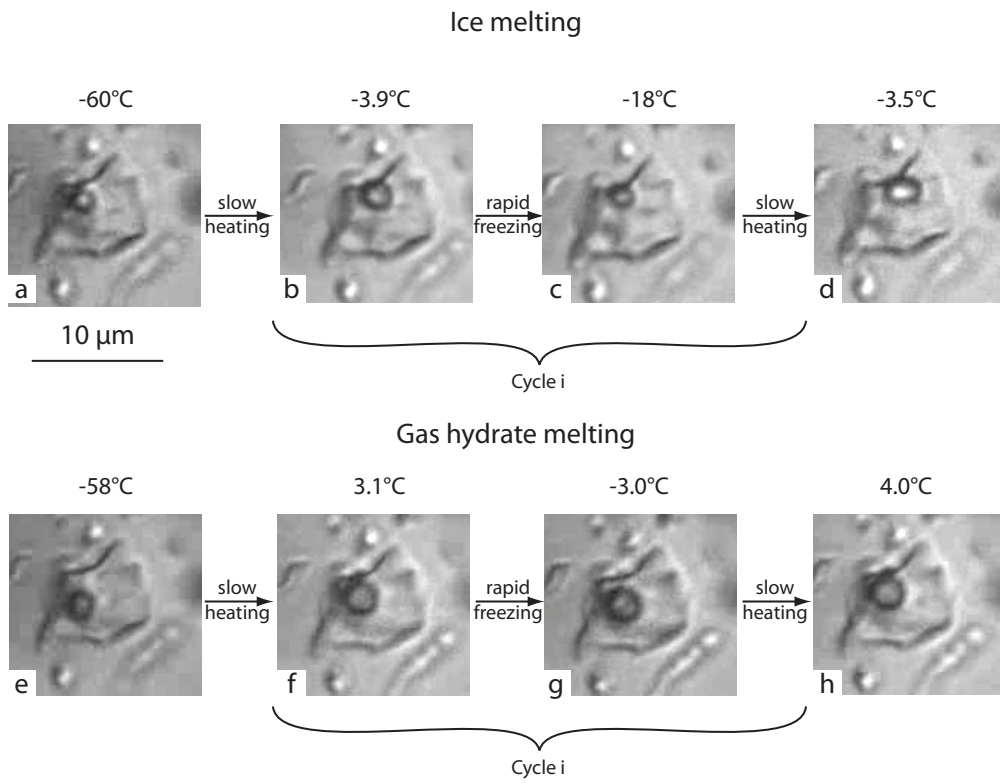


Figure 5:

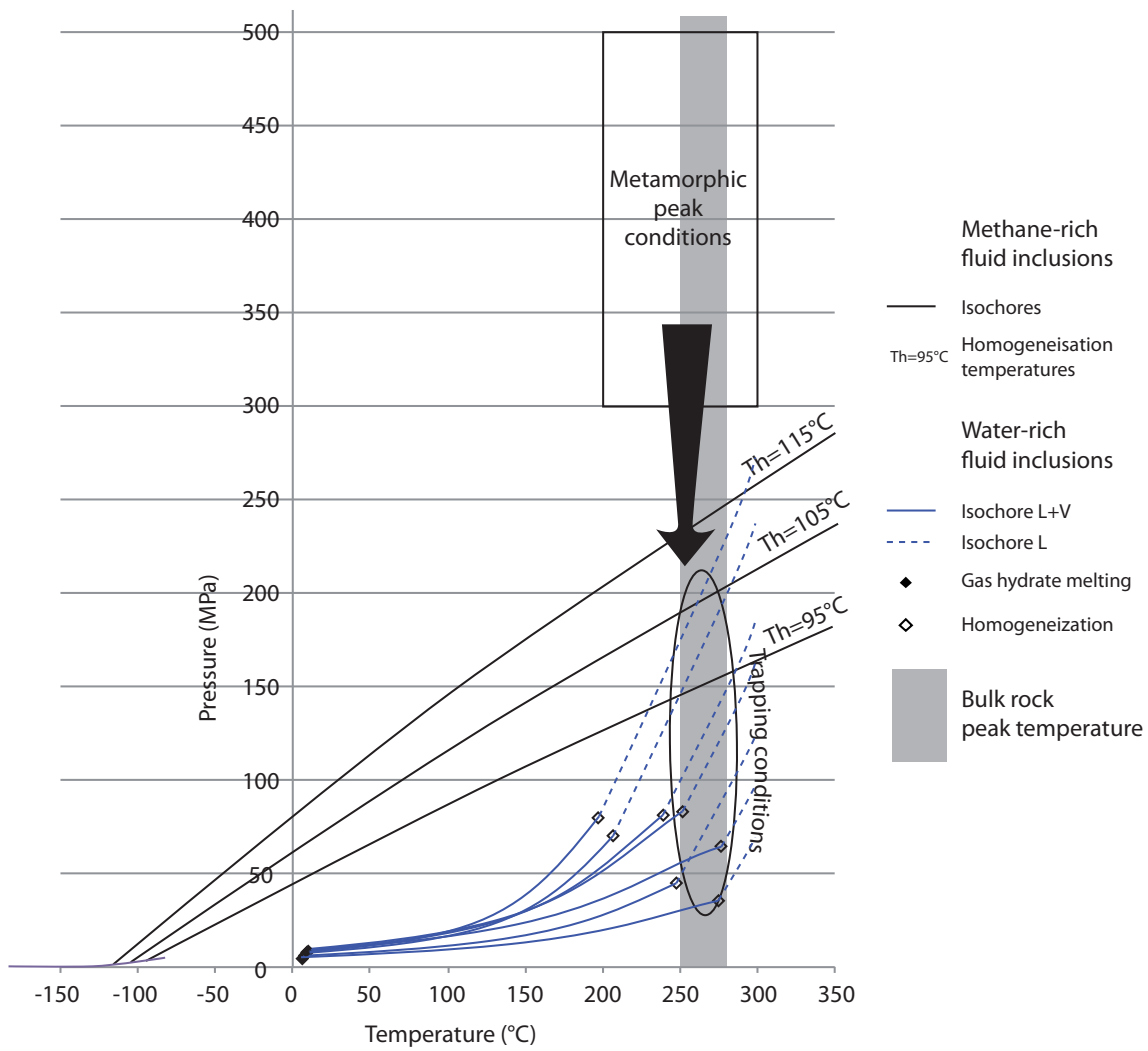


Figure 6:

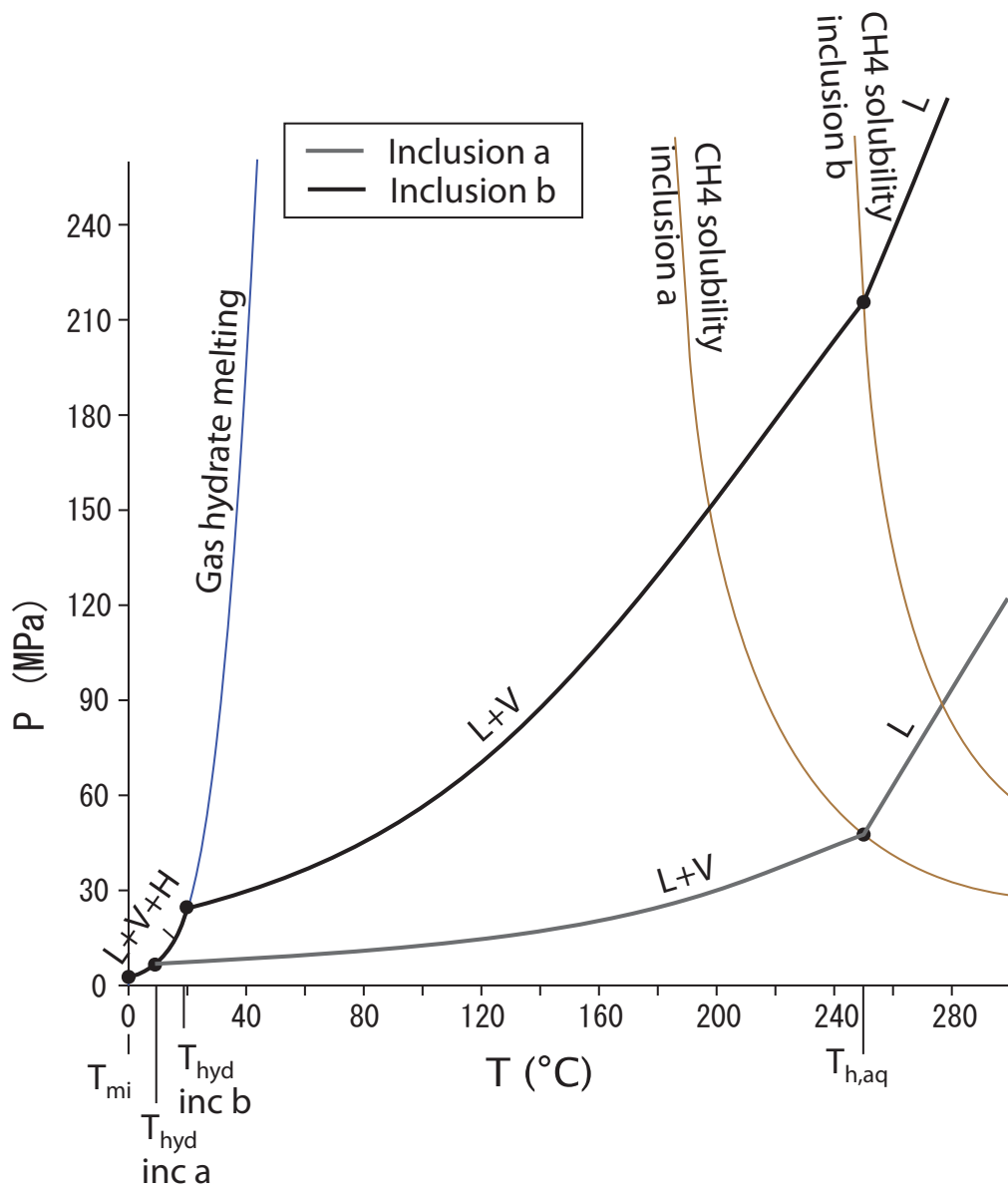


Figure 7: